

Iterative motion-compensation reconstruction ultra-short TE (iMoCo UTE) for high-resolution free-breathing pulmonary MRI

Xucheng Zhu^{1,2}  | Marilynn Chan³ | Michael Lustig^{1,4} | Kevin M. Johnson^{5,6} | Peder E. Z. Larson^{1,2}  

¹UCSF/UC Berkeley Graduate Program in Bioengineering, University of California, San Francisco, California

²Department of Radiology and Biomedical Imaging, University of California, San Francisco, California

³Department of Pediatrics, Division of Pediatric Pulmonology, University of California, San Francisco, California

⁴Department of Electrical Engineering and Computer Sciences, University of California, Berkeley, California

⁵Department of Medical Physics, University of Wisconsin, Madison, Wisconsin

⁶Department of Radiology, University of Wisconsin, Madison, Wisconsin

Correspondence

Peder E. Z. Larson, 1700 4th St, Byers Hall, Room 102C, San Francisco, CA 94143.

Email: peder.larson@ucsf.edu

Twitter: @pezlarson

Funding information

National Institutes of Health (NIH), grant R01 HL136965.

Purpose: To develop a high-scanning efficiency, motion-corrected imaging strategy for free-breathing pulmonary MRI by combining an iterative motion-compensation reconstruction with a ultrashort echo time (UTE) acquisition called *iMoCo UTE*.

Methods: An optimized golden-angle ordering radial UTE sequence was used to continuously acquire data for 5 minutes. All readouts were grouped to different respiratory motion states based on self-navigator signals, and then motion-resolved data was reconstructed by XD golden-angle radial sparse parallel reconstruction. One state from the motion-resolved images was selected as a reference, and then motion fields from the other states to the reference were derived via nonrigid registration. Finally, all motion-resolved data and motion fields were reconstructed by using an iterative motion-compensation (MoCo) reconstruction with a total generalized variation sparse constraint.

Results: The iMoCo UTE strategy was evaluated in volunteers and nonsedated pediatric patient (4–6 years old) studies. Images reconstructed with iMoCo UTE provided sharper anatomical lung structures and higher apparent SNR and contrast-to-noise ratio compared to using other motion-correction strategies, such as soft-gating, motion-resolved reconstruction, and nonrigid MoCo. iMoCo UTE also showed promising results in an infant study.

Conclusion: The proposed iMoCo UTE combines self-navigation, motion modeling, and a compressed sensing reconstruction to increase scan efficiency and SNR and to reduce respiratory motion in lung MRI. This proposed strategy shows improvements in free-breathing lung MRI scans, especially in very challenging application situations such as pediatric MRI studies.

KEYWORDS

free breathing, motion compensation, pediatric imaging, pulmonary imaging

1 | INTRODUCTION

MRI has the potential to assess pulmonary diseases by providing soft-tissue contrast and structural information within the lung.¹ Compared to CT scanning, MRI avoids ionizing radiation exposure, which would be safer for pediatric subjects² or patients requiring longitudinal follow-up imaging.³ However, pulmonary MRI is challenging due to short T_2^* , low proton density of the lung parenchyma,^{4,5} and subject motion—especially respiratory motion.⁶

Ultrashort TE (UTE)-⁷ and zero TE (ZTE)-type⁸ acquisition strategies have been developed that preserve short T_2^* signal in the lung by providing the means to collect images with a sub-millisecond TE. Such sequences use optimized excitation pulses and readouts strategies to maximize SNR for pulmonary imaging⁹; however, most UTE/ZTE sequences still take a few minutes or longer, usually 5 to 10 minutes,^{5,10,11} which is required to obtain sufficient lung parenchyma SNR with high spatial resolution. During the scan, there are inevitable motion effects, especially from respiratory motion. In addition, longer scan time increases the possibility of irregular motion of the subject, especially for pediatric subjects¹² and subjects with poor pulmonary function.

A variety of respiratory motion-compensation (MoCo) strategies have been developed, most of which utilize motion tracking for retrospective motion correction or compensation. External respiratory belts are widely used to indirectly track the motion by measuring the respiratory-induced abdomen stretching. An alternative way is to use the repeatedly acquired k-space center also referred to as direct current (DC) signal, which is feasible for center-out UTE sequences, measuring the signal change caused by respiratory motion.^{7,11,13,14} To more accurately and directly characterize subject motion, low spatial but high temporal resolution 2D/3D images could be reconstructed and used as a self-navigator.^{6,15-17}

Most of the motion-correction and MoCo methods can be classified into 3 categories: The first is respiratory gating. Based on the respiratory motion signal, only data acquired within a certain motion state, usually the end expiratory state, is used for reconstruction.¹⁸ However, gating-based methods reduce scan efficiency and prolong the scan time. To increase the scan efficiency, the soft-gating method was proposed to add nonzero weightings on the data,^{6,19,20} but it reduces the ability to correct motion.¹⁰ The second is motion-resolved reconstruction. Instead of reconstructing a single motion-gated image, all acquired data are grouped in different motion states, and spatial-correlation of the different images is used as the prior information for compressed sensing-based reconstruction such as XD golden-angle radial sparse parallel reconstruction (XD-GRASP)^{21,22} and kt-focal underdetermined system solve (kt-FOCUSS).²³ The third is MoCo reconstruction with image registration. Unlike gating or soft-gating strategies, MoCo strategies align all motion

states images to the same state via image-based registration. After registration, all motion states images are summed to compose a single image, therefore increasing the data acquisition efficiency.²⁴ MoCo-type strategies have been applied in simultaneous PET/MR applications for increased PET image SNR.²⁵⁻²⁹ A more sophisticated way that Batchelor et al³⁰ first proposed is the generalized matrix description to formulate the motion deformation as a matrix operator to describe the motion propagation in signal space. A few MoCo reconstruction strategies³¹⁻³⁵ based on generalized matrix description have been proposed and applied to cardiac MRI.

In this work, we propose a new free-breathing motion-corrected pulmonary MRI strategy, iterative MoCo reconstruction UTE, called *iMoCo UTE*, to improve high spatial resolution free-breathing lung MRI. There are 3 main components of the proposed method: 1) a pseudo random non-Cartesian UTE sequence, 2) motion-resolved reconstruction and motion estimation, and 3) a novel iMoCo reconstruction with compressed sensing. The iMoCo reconstruction iteratively fits the data to a nonrigid motion model and leverages compressed sensing principles to further suppress noise and artifacts. When combined with a UTE sequence, the proposed method addresses the challenges in lung MRI of intrinsically low SNR and motion by providing a high acquisition efficiency and motion robust pulmonary MR images, especially in challenging situations such as pediatric MRI studies. The proposed strategy is evaluated on both healthy volunteers and pediatric patients and compared to other motion correction strategies, such as soft-gating, motion-resolved reconstruction, and image-based MoCo strategies.

2 | METHODS

2.1 | Overview workflow of iMoCo UTE

The overall workflow of proposed iMoCo UTE is summarized in Figure 1. Data are acquired with a pseudo randomly sampled 3D radial UTE sequence, which results in k-space sample ordering being uncorrelated with the respiratory motion. Then, data are binned to different motion states according to respiratory tracking signals. Respiratory tracking is first determined using a k0/DC navigator signal. Then, additional image-based navigator is used to remove the data with irregular motion (Figure 1A). Instead of doing high spatial resolution motion-resolved reconstruction, the motion-resolved data is used first to reconstruct ~1.5 times coarser spatial resolution motion-resolved images (Figure 1B). Motion fields from different motion states to a reference state are then estimated via nonrigid registration³⁶ (Figure 1C). Finally, the estimated motion fields and a spatial total generalized variation (TGV) sparsity constraint³⁷ are added into the iMoCo reconstruction model to reconstruct a single-state high-resolution motion-free image.

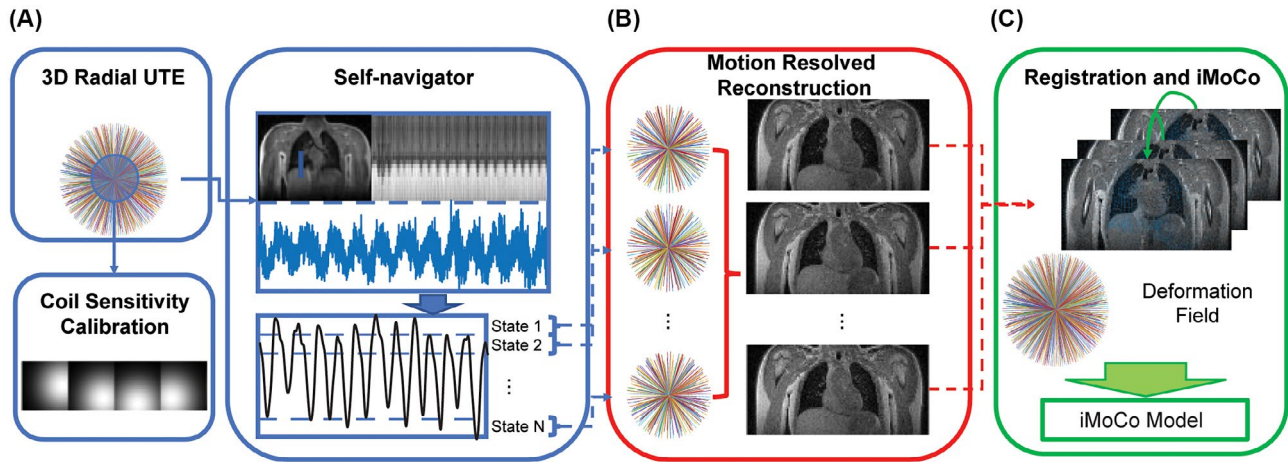


FIGURE 1 Overview of the iMoCo UTE workflow. (A) After optimized 3D radial UTE data are acquired, the center k-space is cropped out for coil sensitivity calibration and then used to estimate the respiratory motion signal via the k0 signal or a reconstructed 3D image navigator. (B) Based on the self-navigator signal, data are grouped in different motion states, and then motion-resolved images with medium spatial resolution are reconstructed. (C) All motion states images are registered to the selected reference state image via nonrigid image registration, and then the deformation fields and the whole dataset are fed in the iMoCo reconstruction model. iMoCo, iterative motion-compensation; UTE, ultrashort TE

2.2 | UTE sequence

An optimized 3D UTE sequence with slab selection and variable density readout acquisition,⁹ which increases the SNR efficiency and reduces aliasing artifacts, was used for pulmonary imaging scans. A golden-angle ordering acquisition scheme was used to randomize undersampling artifacts over time and improve the motion-resolved reconstruction and motion estimation. All of the studies were performed on 3T MRI clinical scanners (MR750, GE Healthcare, Waukesha, WI). More specific acquisition parameters are listed in the experiment section.

2.3 | Respiratory motion detection and motion-resolved reconstruction

A DC-based self-navigator was used for initial respiratory motion detection in which the first points of the radial readouts are used as self-navigator signals. The multichannel data were combined via the adaptive navigator strategy.³⁸ Then, DC signals were filtered by low-pass (0.5~1 Hz cutoff frequency) filter to reduce high-frequency noise. The DC navigator was used as long as no large fluctuation of the DC signal (defined as having a signal deviation from baseline that was 3 times greater than range of the respiratory signal) was observed. If there was a baseline fluctuation of the DC signal, alternatively, a 3D image-based navigator, generated by a locally low rank-constrained reconstruction,⁶ was used to identify and discard bulk motion corrupted data. The respiratory motion signal was derived from the DC signal after discarding the irregular motion corrupted data and baseline correction. (The 3D image navigator was not used for respiratory motion estimation due to limitations on the spatial

[~3 mm isotropic] and temporal resolution [~300 ms] that were not sufficient to capture pediatric respiratory motion.)

Based on the motion estimates, the acquired data was binned into different respiratory motion states for motion-resolved reconstruction, a process similar to XD-GRASP.²¹ Even when data are binned into different motion states, there is inevitable residual motion among data within the same motion state. To minimize this effect, a large number of motion states—between 8 and 10—were used. This is in contrast to standard XD-GRASP, which typically uses 4 to 6 motion states.²² However, because the full dataset (all spokes) are usually 3- to 4-fold undersampled, if number of motion states increases to 8 or higher, the undersampling factor would go up to 30, which would lead to strong streaking artifacts and lower SNR even with compressed sensing and parallel imaging. To accommodate the higher undersampling and reduce the reconstruction artifacts, a coarser resolution (~1.5 times the native resolution) was used, which maintains a reasonable undersampling factor in this workflow. Because the purpose of the binning is for estimation of motion between the bins and correction for it, a full-resolution reconstruction is not necessary. Reducing the resolution has the added benefit of reducing the computational load. The reconstruction was done via an XD-GRASP-type reconstruction solving,

$$\argmin_X \sum_{i,k}^{N,m} \left\| W (F S_i X_k - d_{ik}) \right\|_2^2 + \lambda_s \|\Phi X\|_1 + \lambda_t TV_t(X). \quad (1)$$

Here, the squared-error data consistency term (left) includes multichannel sensitivity maps S_i ($i = 1, 2, \dots, N$) and motion states-sorted multi-channel data d_{ik} ; W is sampling density-compensation weights; F is the nonuniform Fourier transform operator implemented via gridding algorithm; and X_k are the

motion-state 3D images parametrized by motion state index k . A spatial sparsity 3D 11-wavelet term for which Φ is the wavelet transform and a motion dimension total variation term, $TV_t()$, are added to the reconstruction. Additional motion-resolved reconstruction formulations, which include removing the spatial 11-wavelet term or replacing it with spatial total variation, were also evaluated as described in the Supporting Information Figure S1. Following the motion-resolved reconstruction, 1 of the motion states (e.g., typically the end expiratory state) was selected as a reference frame. All other motion state images were then registered to the reference via Demons nonrigid registration³⁶ (4 pyramid levels, coarse-to-fine registration, and 100 iterations are used in Demons). Estimated motion fields were interpolated to match the full-resolution image and used in the following MoCo reconstruction.

2.4 | Iterative motion-compensated reconstruction

Once the motion fields were derived, the entire data is used to reconstruct a single frame, which is motion-corrected. We leverage the relation that $M_k \hat{X} = X_k$, for which M_k ($k = 1, 2 \dots m$) are derived motion fields and that \hat{X} is the final reconstructed image, to include our motion estimates in the forward model. As described in the generalized matrix description model, the motion field can be formulated as a linear operator. Although the inverse operator of nonrigid deformation is difficult to calculate, the adjoint operator can be simply estimated as reverse deformation from the reference to a certain state image. To further reduce streaking artifacts caused by undersampling and residual motion, a spatial TGV sparsity regularization term is added to the model. Unlike spatial total variation regularization, TGV relaxes the assumption that image is piecewise constant, which would be more suitable for continuous signal changes of tissues.³⁷ Thus, the reconstruction problem can be reformulated as optimization problem:

$$\underset{\hat{X}}{\operatorname{argmin}} \sum_{i,k}^{N,m} \left\| W(FS_i M_k \hat{X} - d_{ik}) \right\|_2^2 + \lambda_s \operatorname{TGV}_s(\hat{X}). \quad (2)$$

In the data consistency term (left), I , d_{ik} , and F are the same notations as the motion-resolved reconstruction (Equation 1), with the addition of derived motion fields M_k ($k = 1, 2 \dots m$). \hat{X} is the final reconstructed, single-state high-resolution image. The sparse penalty term (right) is $\operatorname{TGV}_s()$. The optimization problem is solved by using first-order primal-dual algorithm.³⁹

2.5 | Experiments

All human studies conducted were approved by University of California, San Francisco, Institutional Review Board.

Several different types of studies are included in the results and discussions.

For adult healthy volunteer studies ($N = 7$), scan parameters included prescribed FOV = $32 \times 32 \times 32 \text{ cm}^3$ ($64 \times 64 \times 64 \text{ cm}^3$; 2-fold oversampling on readout direction for radial sequence); flip angle = 4° ; 1.25 mm or 1 mm isotropic resolution; readout bandwidth = $\pm 125 \text{ kHz}$; TE = 70 μs ; TR = 2.7–3.1 ms; and TR increased as the prescribed FOV was reduced. The total scan time was approximately 5 min to 5 min 30 s. Number of total acquired spokes of each scan was approximately 100 thousand.

For pediatric patients diagnosed with pulmonary diseases studies ($N = 4$), the FOV was prescribed based on the size of the subject (22–26 cm), and spatial resolution (isotropic) was kept to 1.1 mm or higher ($< 1 \text{ mm}$) due to their smaller anatomical structure size. Both TE and TR (TE = 80–110 μs , TR = 3.1–3.7 ms) increased compared to adult studies due to smaller FOV and excitation slab. The number of spokes was adjusted between 80 thousand to 90 thousand to keep the total scan time no more than 5 min 30 s. Due to varied scan subject size, different receiver coil arrays were used in pediatric scans to improve SNR: 8-channel and 32-channel cardiac arrays (GE Healthcare, Waukesha, WI), as well as a 12-channel flexible screen-printed coil array (InkSpace Inc., Moraga, CA).⁴⁰

For the infant patient study ($N = 1$), the following scan parameters were used: FOV was 18 cm; spatial resolution (isotropic) was 0.9 mm; TE = 170 μs ; TR = 4.6 ms; number of spokes was 75 thousand; and total scan time was around 5 min 30 s. Eight-channel head coil (GE Healthcare, Waukesha, WI) was used in the experiment due to very small subject size.

2.6 | Data processing and imaging reconstruction

The self-navigator, motion signal processing, and iMoCo reconstruction were implemented in MatLab 2017a (MathWorks, Natick, MA). Coil sensitivity maps calibration, motion-resolved reconstruction, and soft-gating reconstructions were carried out by the Berkeley Advanced Reconstruction Toolbox (BART).⁴¹ All of the quantitative measurements were also implemented in MatLab (MathWorks).

2.7 | Image quality comparison and evaluation

For image quality comparisons, we implemented nongating, soft-gating, motion-resolved, and nonrigid MoCo reconstruction and motion-correction strategies following the details in previous works.^{6,19,22} Briefly, the MoCo method used the motion-resolved reconstruction from XD-GRASP to generate images across motion states, which were then

nonrigidly registered using Demons and then averaged together. Hyperparameters used were kept the same in all of the reconstructions.

To quantitatively compare the image quality among different motion-correction strategies, several image metrics were computed. The sharpness of the lung–liver interface or diaphragm was measured via the relative maximum derivative (MD), defined as the maximum intensity change between lung–liver interfaces divided by mean intensity in the liver.

Apparent SNR (aSNR), defined as the average signal over a small region of interest divided by the SD of the area out of the subject, was measured. Three representative areas were selected as regions of interest: an airway, the lung parenchyma, and the aortic arch. Instead of SNR, aSNR was measured in this work because the reconstruction methods could introduce spatially varying noise and also perform inherent denoising. Images reconstructed with different strategies were spatially aligned; thus, regions of interest at the same locations could be manually drawn on all of the reconstructed images for measurement.

Contrast-to-noise ratio (CNR), defined as the contrast difference over noise level, was also computed. In lung MRI, it is valuable to distinguish air, lung parenchyma, and vessels. Therefore, CNR between the lung parenchyma and air and between the aortic arch and air was measured.

A paired sample *t* test ($P < 0.05$) method was used for statistical comparison of the quantitative measurements MD, aSNR, and CNR.

3 | RESULTS

3.1 | Volunteer studies comparison

Volunteer study results are shown in Figure 2. One sagittal slice image from 2 adult volunteer studies with the proposed iMoCo and other motion-correction strategies is shown in each of the first rows. The overall image quality of both subjects with iMoCo method is better than motion-resolved and soft-gating methods due to higher data usage efficiency and a more accurate motion model. The zoomed-in images show that the proposed reconstruction has better lung parenchyma

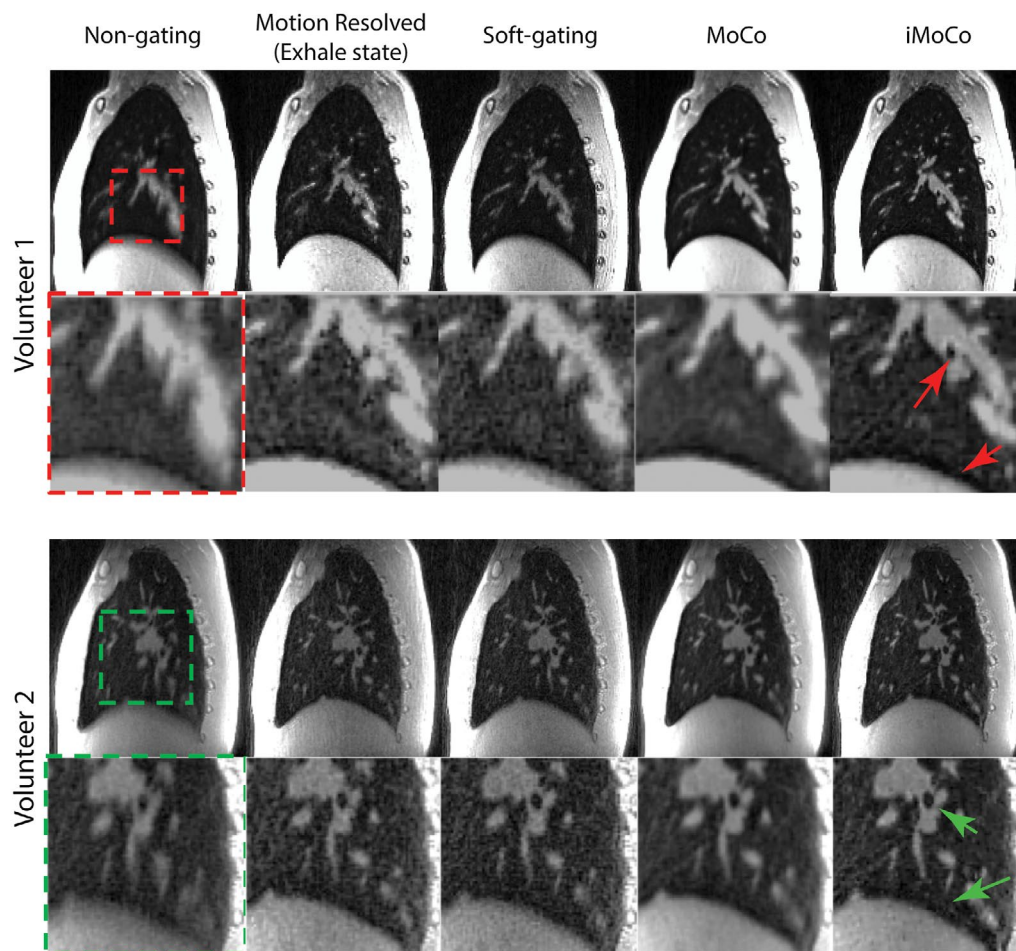


FIGURE 2 Example of volunteer study image results. The same slice images of each subject reconstructed with different motion correction and reconstruction strategies are plotted in the first rows, and dashed squares targeting at the center area of the lung are zoomed in and plotted in the second rows. In both cases, the iMoCo strategy had the sharpest image features and highest apparent SNR

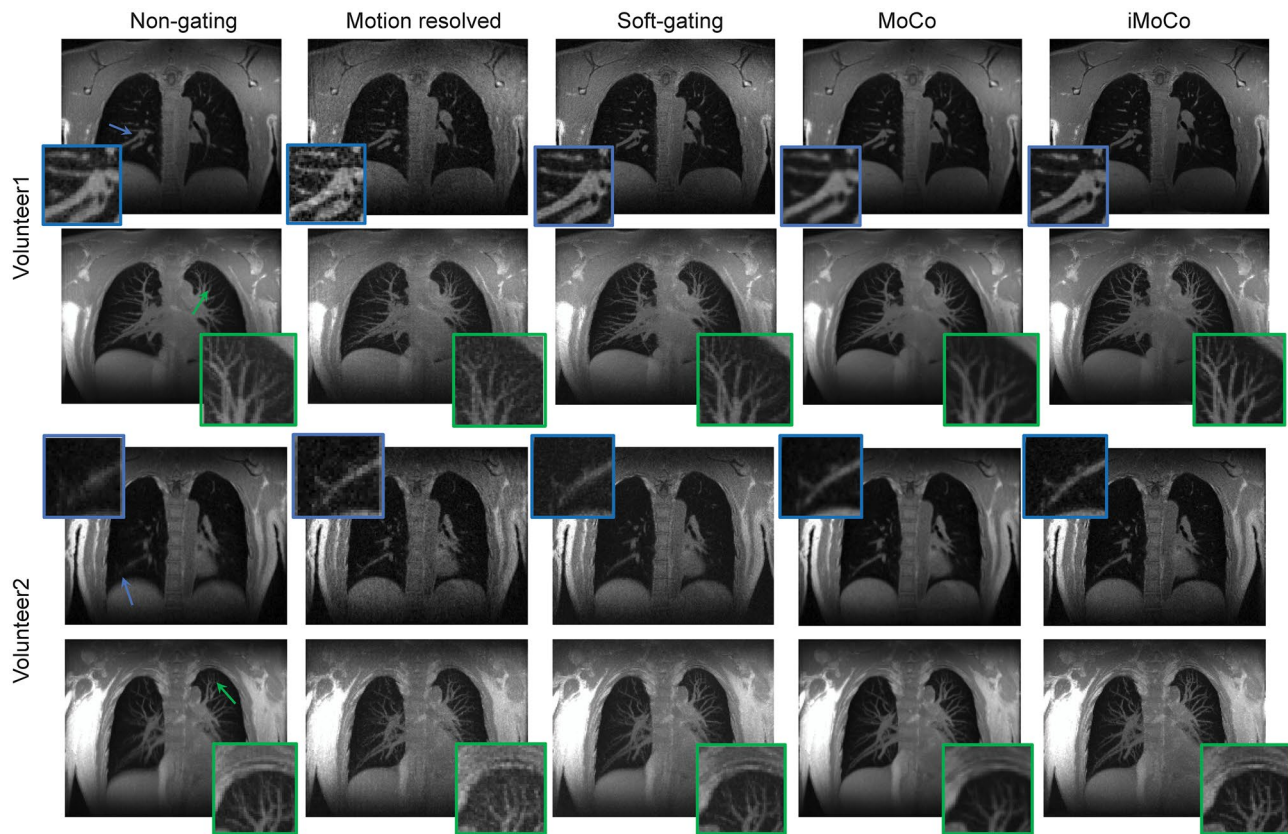


FIGURE 3 Example of high spatial resolution (1 mm isotropic) lung images. The proposed iMoCo reconstruction is compared to nongating, motion-resolved reconstruction (exhale state), soft-gating, and MoCo reconstructions. In each volunteer example, the first row shows the 1 slice from different reconstructed images, and the second row shows the MIP of 30 slices in the anteroposterior direction. The area pointed to by the arrows in the nongating images are zoomed in. The iMoCo reconstruction was able to delineate the smallest pulmonary vessels. MIP, maximum intensity projection; MoCo, motion compensation

contrast and less residual motion compared to the soft-gating method and also has sharper edges of airways and vessels compared to the MoCo method.

To compare the capability to visualize small vessels and airways in the lung, 2 higher spatial resolution (1 mm isotropic resolution vs. 1.25 mm isotropic resolution in Figure 2) examples are shown in Figure 3. One coronal slice from each study is shown in the first row, and a maximum intensity projection of 30 slices centered at the first-row coronal images positions is plotted in the second row. Images with the iMoCo reconstruction have the best visual image quality and show lower noise level, sharper vascular structures, and more small blood vessels compared to other methods.

3.2 | Pediatric patient studies

Pediatric pulmonary MRI studies are much more challenging, especially for nonsedated free-breathing scans. First of all, it is difficult for children to keep still during a long scan. Also, their respiration rates tend to be higher and less regular. In addition, the quiescent period after exhalation is much shorter, which might reduce the SNR efficiency and image

quality of gating- and soft-gating-based methods.¹⁰ Pediatric patients with different types of lung diseases and of different ages were scanned to show the capability of imaging different lung abnormalities with iMoCo UTE. Results of 3 representative pediatric studies with different observed abnormal lung structures are shown in Figure 4. An image slice with the abnormality is shown in the first row, and a zoomed-in image is shown in the second row. Images carried out by different reconstruction algorithms are compared for 3 patients: Patient 1 was a 5-year-old female who had a severe combined immunodeficiency (SCID) post-stem cell transplant with several observed lung nodules (red dashed circles); patient 2 was a 4-year-old male with systemic juvenile idiopathic arthritis and childhood interstitial lung disease (chILD) with observed ground-glass opacity (green dashed circle, this opacity was also observed on CT); and patient 3 was a 8-year-old female with surfactant protein C deficiency who had small pneumatoceles (lung cysts; blue arrow). Images with the iMoCo reconstruction had the best depiction of these pathologic features. Particularly in patient 3, the pneumatocele has a much sharper boundary and better contrast with iMoCo compared to other methods.

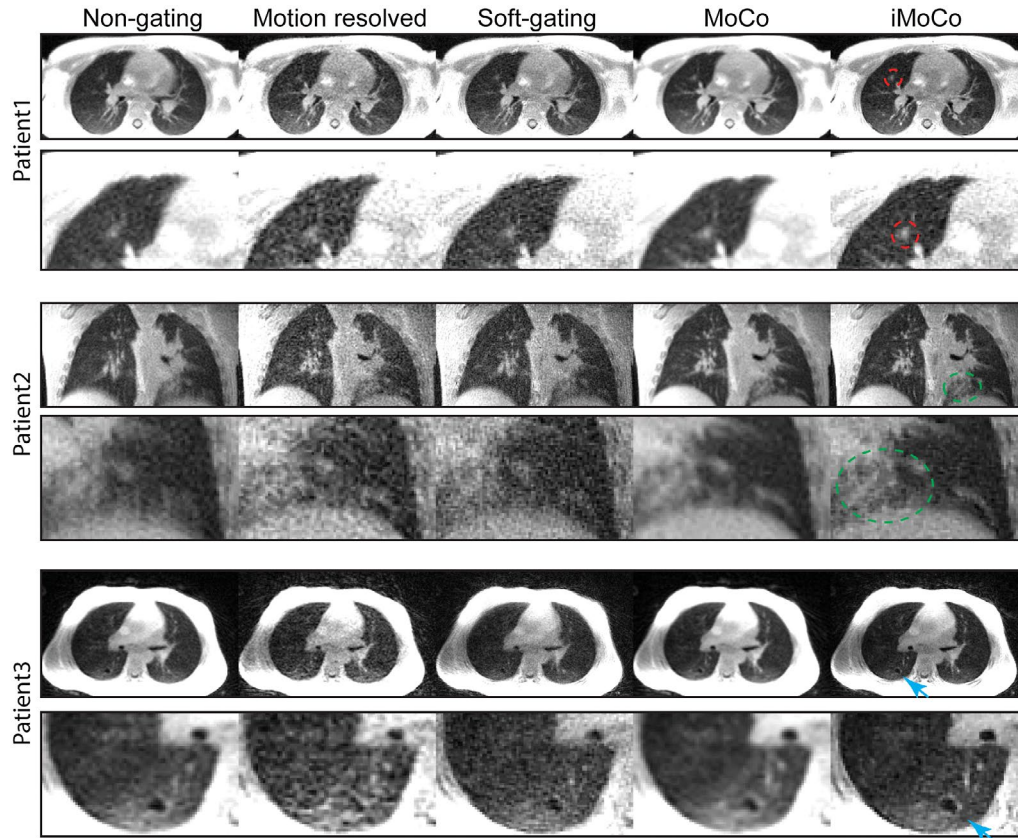


FIGURE 4 Pediatric patient study examples. Three different patient lung UTE scan (1 mm isotropic resolution) results with different motion-correction and -reconstruction strategies are plotted. A lung nodule is pointed out (red dashed circle) in patient 1 (5 years old). A region of ground-glass opacity is shown (green dashed circle) in patient 2 (4 years old). Small pneumatocèles (lung cysts) are pointed out (blue arrow) in patient 3 (8 years old). Abnormality regions of all examples are zoomed in, shown in the second rows. UTE, ultrashort TE

3.3 | Hyperparameters selection

In the proposed iMoCo reconstruction Equation 2, there are 2 tunable hyperparameters: one is number of motion states and the other is TGV regularization weighting. Experiments with different hyperparameters were designed to investigate the selection of hyperparameters for the reconstruction.

iMoCo reconstructions carried out using different numbers of motion states are compared in Figure 5. In the example, the diaphragm motion range was ~ 1 cm; the motion-resolved spatial resolution was 1.5 mm; and the final resolution was 1.25 mm. As the number of motion states increased from 2 to 6, the reconstructions improved, especially close to diaphragm (green arrow); however, trivial improvement was observed as the number increased from 6 to 8. We also quantitatively evaluated the effects from the number of motion states on the final motion correction performance. The diaphragm maximum derivative was used to represent the motion correction performance, plotted in (Figure 5B). Higher MD means better motion correction result. As the number of states increased from 2 to 6, 4 out of 4 cases showed MD increased. As the number of states goes larger, the improvement is inconsistent

among different cases. Therefore, we believe the number of states could be estimated by the motion range divided by the motion-resolved reconstruction resolution (in this example, $1 \text{ cm}/1.5 \text{ mm} = 6.6$). Eight motion states were used in all the results in this work.

In Equation 2, λ_s is the hyperparameter tuned to control spatial TGV regularization term. The reconstruction with TGV regularization will reduce the noise and suppress the undersampling and residual motion artifacts. Reconstructed images with different λ_s are shown in Figure 6 using image data from 1 of the high-resolution studies shown in Figure 3. As λ_s increases, the noise and streaking artifacts are reduced. However, as λ_s increases to 0.1, the overall images look over-smoothed, especially because some small vessels are blurred out, as seen in the green circle area in Figure 6A. Maximum intensity projection of 30 slices is shown in Figure 6B to further compare the effect of λ_s on small structures. $\lambda_s = 0.05$ shows less noisy without sacrificing the small vessels structures. aSNR measurements are used to present quantitatively present the effect of λ_s , where Supporting Information Figure S3 shows the aSNR change from airway, lung parenchyma, and aortic arch as λ_s increases. Although all the aSNRs increase

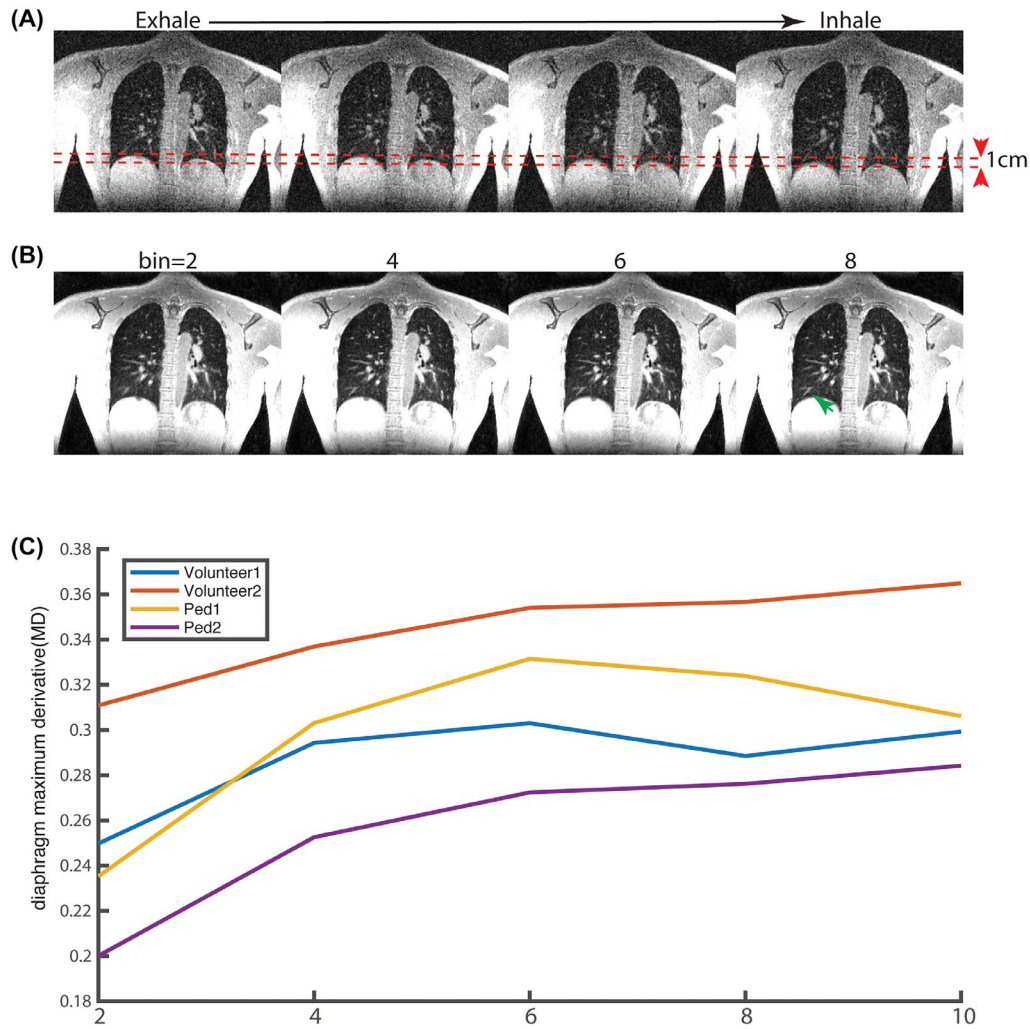


FIGURE 5 Effect of the number of motion states on the iMoCo reconstruction. An example in a healthy volunteer is shown. A motion-resolved reconstruction (8 motion states) is shown in (A), where the diaphragm motion from exhale to inhale state is ~1 cm. The iMoCo reconstructions with different motion states bin numbers are plotted in (B). Diaphragm MDs from 4 cases (2 from volunteers, 2 from pediatric patients) reconstructed via iMoCo using different number of motion states are plotted in (C). MD, maximum derivative

along λ_s , aSNR in airway is expected to be 0, which indicates that λ_s goes to 0.1 or higher is overregularized. Therefore, λ_s was set to 0.05 for the iMoCo reconstructions.

3.4 | Quantitative measurement

For all volunteer ($n = 7$) and pediatric patient ($n = 4$) studies, we quantitatively measured the MD on 10 sagittal slices with different motion correction strategies and normalized the MD to the mean liver signal intensity close to the diaphragm. Measurements are summarized in Figure 7. Images carried out by iMoCo methods show significantly higher MD value compared to nongating, soft-gating, and MoCo methods. Six of 11 subjects had the highest diaphragm MD with iMoCo reconstruction.

We also measured the aSNR and CNR of certain regions in the lung, and the results are summarized in Figure 8. The

aSNR in airways is expected to be close to 0 because there is very little ^1H density in air, and aSNR in lung parenchyma and aorta approximate the SNR level of short and long T_2^* tissues, respectively, with the reconstruction methods. The aSNR increase in MoCo images can be attributed to the lower apparent spatial resolution due to smoothing effects induced by the deformation interpolation, which can be observed in the image results in Figures 2 through 3. Images with iMoCo reconstruction have higher lung parenchyma and aortic arch aSNR compared to motion-resolved and soft-gating reconstructions. In addition, the airway aSNR with iMoCo is relatively low, which would benefit distinguishing airways from lung parenchyma. In Figure 8C, iMoCo has significant higher CNR of the lung parenchyma and aortic arch compared to soft-gating and motion-resolved reconstructions.

These quantitative measurements indicate that iMoCo method can not only achieve higher aSNR but can also reduce

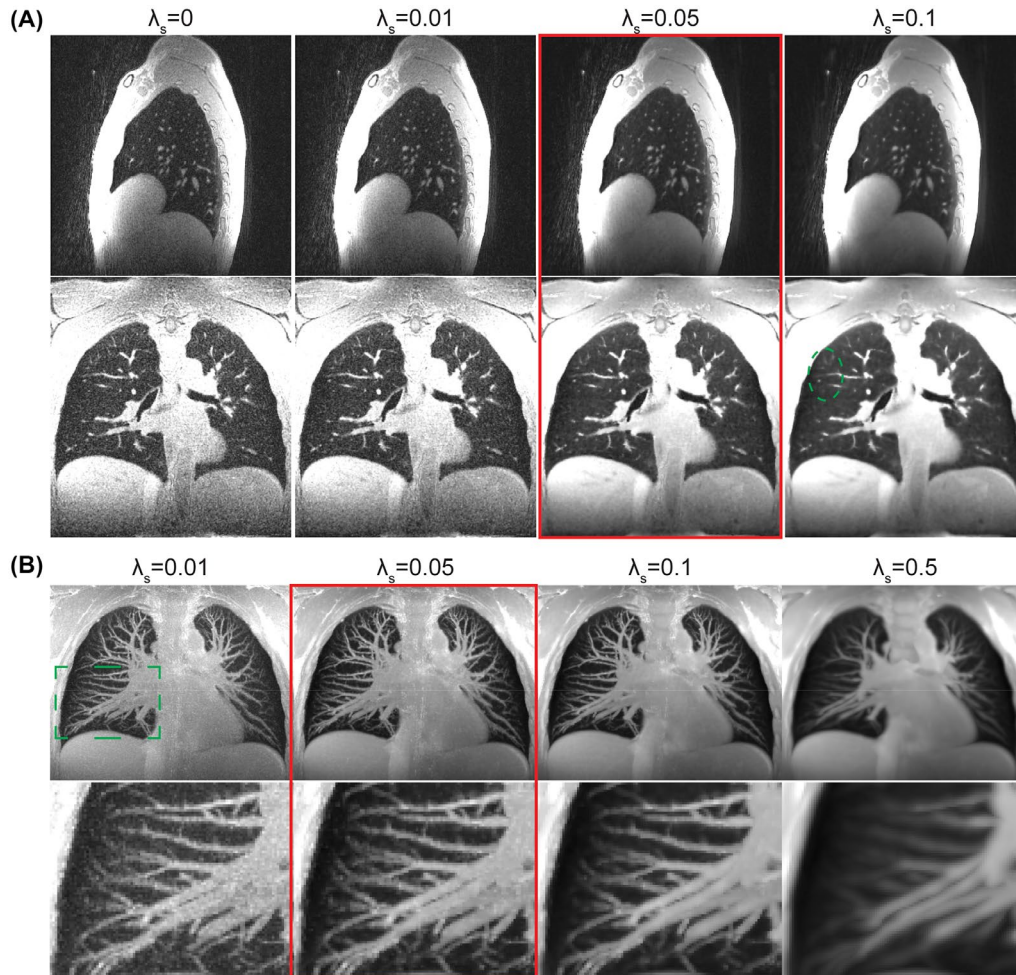


FIGURE 6 Effect of TGV sparse constraint parameter λ on the iMoCo reconstruction. A sagittal and a coronal slice from a healthy volunteer with different TGV constraint parameter λ , from 0 to 0.1, are shown in (A). MIPs of 20 coronal slices of the reconstructed volume with different regularization levels are shown in (B). The first row shows the MIP images, and the second shows the zoomed-in image of the rectangular area in the first image. MIP, maximum intensity projection; TGV, total generalized variation

respiratory motion artifacts, which would benefit the relatively low SNR found in lung MRI.

3.5 | Feasibility of infant study

The significance and feasibility of infant and neonatal lung MRI studies have been reported in previous work.^{12,42,43} High spatial resolution and sufficient SNR are required to visualize smaller structures of the lungs. Figure 9 shows one 5-minute UTE scan of an unsedated 10-week-old infant with pulmonary interstitial glycogenosis (PIG) with 0.9 mm isotropic resolution case. Vessel structures (red arrow) and airways (green arrows) are largely improved with iMoCo reconstruction compared to other methods. An image-based navigator⁶ was also used in this study to capture the bulk motion of the baby; then, the data corrupted by bulk motion were rejected, as shown in Figure 9B. Image results with bulk motion rejection shows sharper vessels and diaphragm (red arrows) compared to without bulk motion rejection, as shown in Figure 9C.

iMoCo with the same hyperparameters was used for both Figure 9C reconstructions.

4 | DISCUSSION

In this work, we proposed a new motion correction strategy by combining UTE, MoCo, and a compressed sensing reconstruction to achieve high-resolution free-breathing lung MRI called *iMoCo UTE*. Although soft-gating type reconstruction strategies have been widely used, they inevitably suffer from the residual motion in the reconstruction data. As the desired reconstructed spatial resolution goes higher, fine structure cannot be reconstructed due to this residual motion. The other option is to use a motion-resolved type reconstruction, for which all data are binned to different motion states, and then use spatial similarity across different motion states to reduce the downsampling artifacts. On one hand, as the number of bins increases the residual motion would

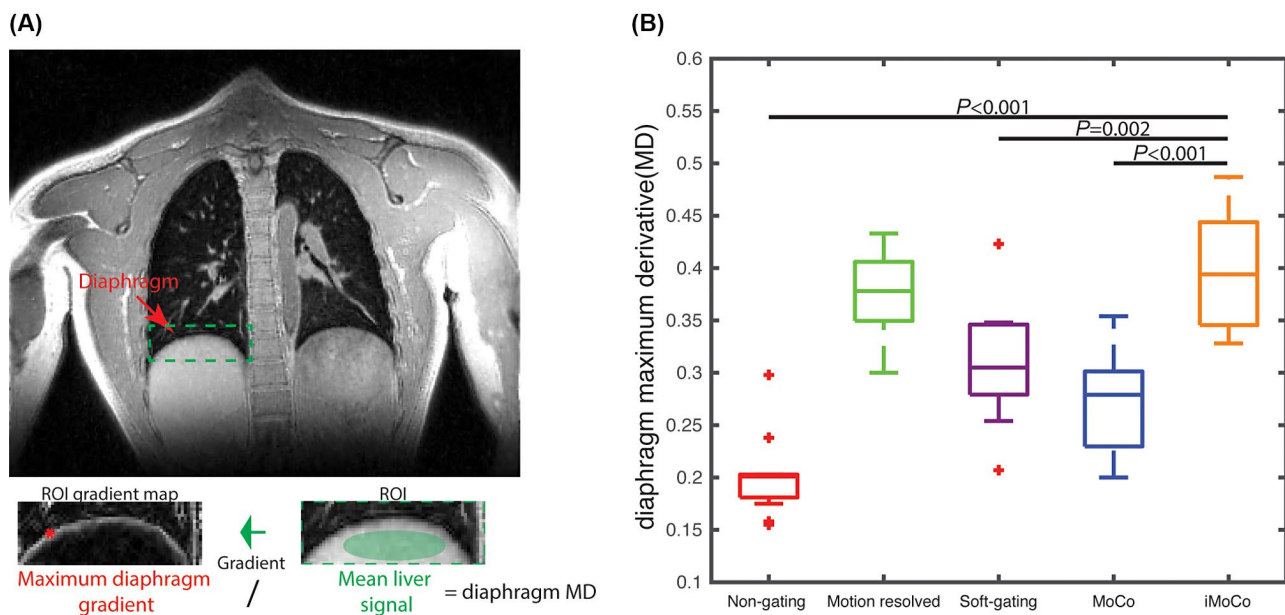


FIGURE 7 Diaphragm MD comparison in which a higher MD corresponds to a sharper edge. The MD calculation process is shown in (A). A MD comparison evaluated on 11 subjects (7 adult volunteers, and 4 pediatric patients) across different methods is plotted in (B). MD, maximum derivative

reduce. On the other hand, a higher undersampling factor in each bin would induce undersampling artifacts. iMoCo aims to model the respiratory motion effects and incorporate spatial motion compensation instead of directly weighting data or segmenting data. Through volunteers and pediatric patient studies, iMoCo shows the capability to achieve high-resolution, high SNR lung images without inducing motion artifacts. According to the quantitative comparison, the iMoCo and motion-resolved reconstructions have the highest MD, and iMoCo and MoCo have higher aSNR compared to other methods. In addition, iMoCo is a general motion correction and reconstruction framework; therefore, it could be extended to other applications and is compatible with different trajectory designs.

4.1 | Motion-resolved reconstruction and motion fields estimation

As mentioned in the results, the number of motion states in motion-resolved reconstruction determines the intrabin residual motion, which would significantly affect the final reconstruction. However, iMoCo also largely depends on the motion field estimation. More motion states might degrade the motion-resolved reconstruction images, leading to image registration errors. iMoCo also depends on accurate motion field estimation; errors in the motion field would propagate to the final reconstructed image, causing blurring or ghosting artifacts.

Previous UTE lung studies have reconstructed 4 to 6 motion states in motion-resolved reconstruction, with an approximately

2-fold undersampling rate overall that resulted in an approximately 10-fold undersampling rate in each motion state data.^{6,22} For the motion-resolved reconstruction this work, we increased the number of motion states to reduce the intrabin motion and also used a slightly coarser spatial resolution to reduce the undersampling rate. This was aimed to ensure that the reconstructed image quality would not degrade the motion fields estimation and following iMoCo reconstruction. We set the motion-resolved reconstruction to 1.5-mm isotropic resolution to keep the undersampling rate in single motion state under or around 10, as the number of motion states was set up to 12, while providing images that could distinguish interbin motion as small as 1.5 mm. In addition, we also compared different image registration methods, and Demons showed the best performance among the methods. An example is showed in Supporting Information Figure S2.

The regularization terms and values for the motion-resolved reconstruction in Equation 1 were chosen empirically based on qualitative evaluation. We also evaluated the effects on motion field estimation by using different regularizations in motion-resolved reconstruction, which are summarized in the Supporting Information Tables S1 and S2. We calculated the RMSE of 2 different motion state images before and after registration, and the linear correlation coefficient and mean Euclidean distance between motion fields derived from different motion-resolved reconstructions. The results were very similar between the different choices of regularization, which indicates that the motion estimation is insensitive to the choice of regularization terms. There also may be room to improve the proposed

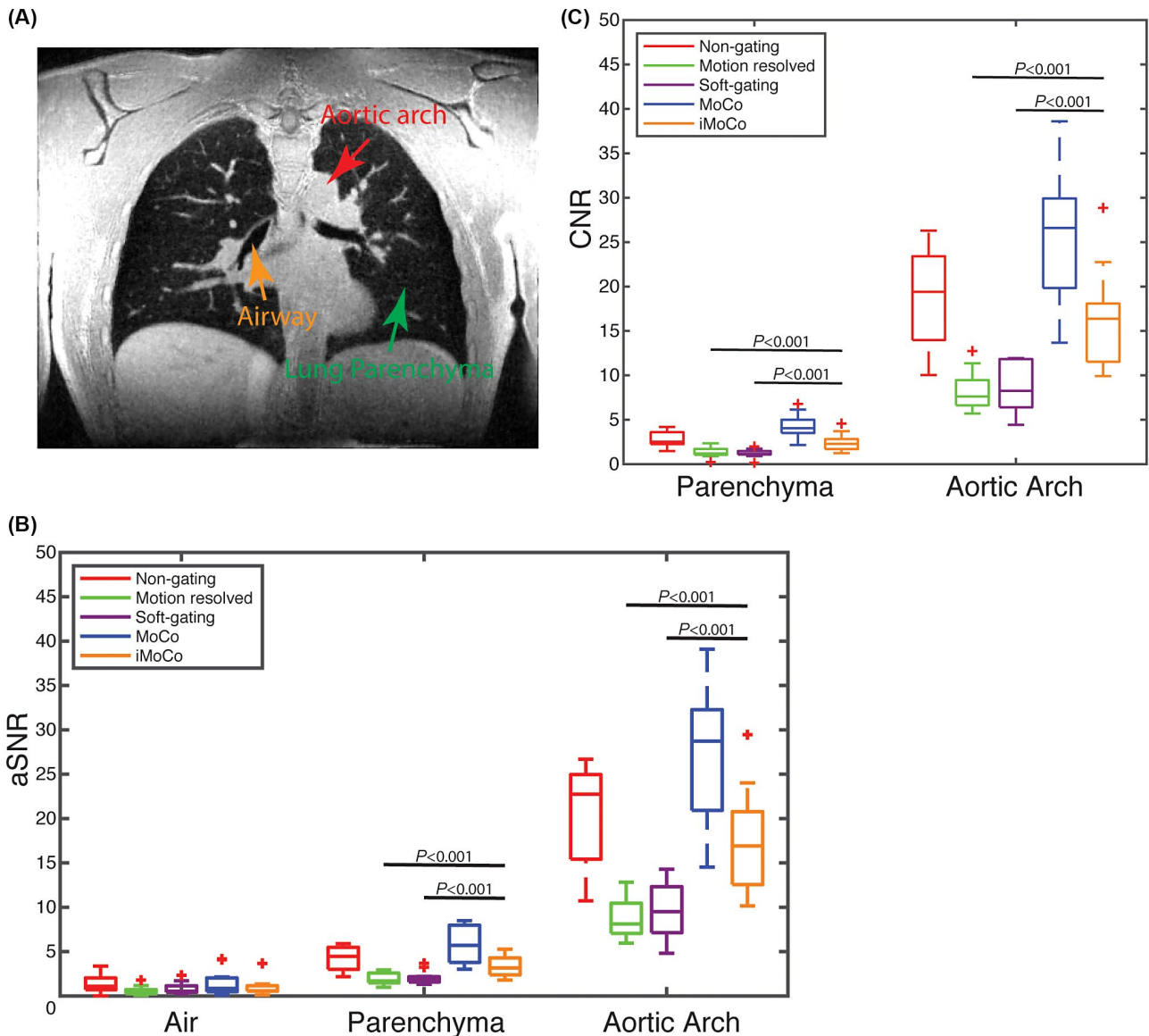


FIGURE 8 aSNR and CNR comparison between the reconstruction methods. Three different anatomical structures, a major airway, the representative lung parenchyma, and the aortic arch were manually annotated for aSNR and CNR measurements. An example of anatomical structures used for the measurements is shown in (A). Comparison of aSNR and CNR is separately plotted in (B) and (C). The increase in aSNR for the MoCo can be partially attributed to a loss of resolution due to smoothing in the reconstruction, which can be observed in Figures 2-4. iMoCo had significantly higher parenchyma and aorta aSNR and CNR compared to motion-resolved and soft-gating reconstructions. aSNR, apparent SNR; CNR, contrast-to-noise ratio

method through more sophisticated techniques, such as locally low-rank constraints,⁴⁴ which also could improve the overall iMoCo method.

In this work, we used 1-to-1 image registration between pairs of motion state images, and registration error might be further reduced by using group-wise registration. All the motion states images could be registered simultaneously, which might improve the robustness of registration process by taking advantage of the registration correlation among the motion states; some work has shown promising results in 4D CT applications.⁴⁵

4.2 | 3D navigator and irregular motion handling

In this work, the self-navigator signals are simply used for respiratory motion binning. By using more sophisticated techniques, a 3D image-based navigator could be extracted and then used to detect the bulk motion or irregular motion. In this work, data contaminated with bulk motion is discarded,^{6,12} which reduces the scan efficiency. We might also be able to incorporate bulk motion or even more complicated irregular motion into iMoCo reconstruction, which

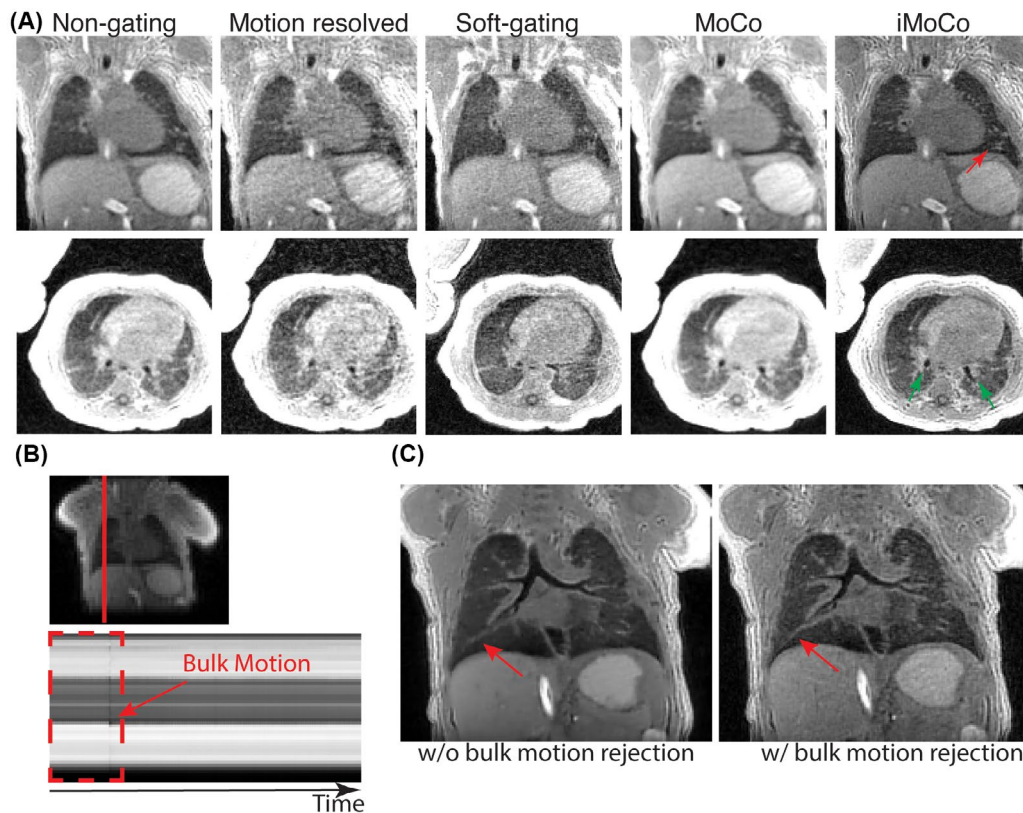


FIGURE 9 10-week-old infant study results. (A) One coronal and 1 axial slice reconstructed with different motion correction and reconstruction strategies (with bulk motion rejection) are plotted. Vessels (red arrow) and airways (green arrows) are pointed out on the iMoCo images, showing improved delineation and contrast compared to other methods. (B) Bulk motion of the infant during the 5-minute scan was detected by an image-based navigator; therefore, data acquired prior to the bulk movement (red dashed rectangle time window) were rejected. (C) Images reconstructed by using iMoCo with and without bulk motion rejection are shown in which bulk motion rejection further reduces the motion effects

might increase the scan efficiency and robustness to irregular motion.

4.3 | Respiration-related pulmonary abnormalities

Some pulmonary abnormalities such as air trapping might lead to intensity changes during respiration.⁴⁶ One of the limitations of our studies is that iMoCo did not include signal intensity changes in the models, which may lead to missing the dynamic change of the abnormalities during respiration.

5 | CONCLUSION

In this work, we proposed a new free-breathing high-resolution pulmonary MRI strategy combining motion compensation, UTE, and compressed sensing, called *iMoCo UTE*. iMoCo UTE has been validated and evaluated via both volunteers and patient studies and shows potential in pediatric and infant pulmonary MRI studies.

ACKNOWLEDGMENT

The authors would like to acknowledge Frank Ong, PhD, and Scott K/ Nagle, MD/PhD, for helpful discussion. The work is supported by National Institutes of Health (NIH) grant R01 HL136965.

ORCID

Xucheng Zhu  <https://orcid.org/0000-0002-5537-5542>

Peder E. Z. Larson  <https://orcid.org/0000-0003-4183-3634>

REFERENCES

1. Togao O, Tsuji R, Ohno Y, Dimitrov I, Takahashi M. Ultrashort echo time (UTE) MRI of the lung: assessment of tissue density in the lung parenchyma. *Magn Reson Med*. 2010;64:1491–1498.
2. Krohmer S, Meier K, Sorge I, Hirsch W, Till H, Weber D. MRI of the lungs in children. *Eur J Radiol*. 2008;68:278–288.
3. Pearce MS, Salotti JA, Little MP, et al. Radiation exposure from CT scans in childhood and subsequent risk of leukaemia and brain tumours: a retrospective cohort study. *Lancet*. 2012;380:499–505.

4. Yu J, Xue Y, Song HK. Comparison of lung T2* during free-breathing at 1.5 T and 3.0 T with ultrashort echo time imaging. *Magn Reson Med*. 2011;66:248–254.
5. Larson P, Johnson KM, Hope MD, et al. Detection of small pulmonary nodules with ultrashort echo time sequences in oncology patients by using a PET/MR system. *Radiology*. 2015;278:239–246.
6. Jiang W, Ong F, Johnson KM, et al. Motion robust high-resolution 3D free-breathing pulmonary MRI using dynamic 3D image self-navigator. *Magn Reson Med*. 2018;79:2954–2967.
7. Holmes JE, Bydder GM. MR imaging with ultrashort TE (UTE) pulse sequences: basic principles. *Radiography*. 2005;11:163–174.
8. Weiger M, Brunner DO, Dietrich BE, Müller CF, Pruessmann KP. ZTE imaging in humans. *Magn Reson Med*. 2013;70:328–332.
9. Johnson KM, Fain SB, Schiebler ML, Nagle S. Optimized 3D ultrashort echo time pulmonary MRI. *Magn Reson Med*. 2013;70:1241–1250.
10. Zucker EJ, Cheng JY, Haldipur A, Carl M, Vasanaawala SS. Free-breathing pediatric chest MRI: performance of self-navigated golden-angle ordered conical ultrashort echo time acquisition. *J Magn Reson Imaging*. 2018;47:200–209.
11. Delacoste J, Chaptinel J, Beigelman-Aubry C, Piccini D, Sauty A, Stuber M. A double echo ultra-short echo time (UTE) acquisition for respiratory motion-suppressed high-resolution imaging of the lung. *Magn Reson Med*. 2018;79:2297–2305.
12. Higano NS, Hahn AD, Tkach JA, et al. Retrospective respiratory self-gating and removal of bulk motion in pulmonary UTE MRI of neonates and adults. *Magn Reson Med*. 2016;77:1284–1295.
13. Weick S, Völker M, Hemberger K, et al. Desynchronization of Cartesian k-space sampling and periodic motion for improved retrospectively self-gated 3D lung MRI using quasi-random numbers. *Magn Reson Med*. 2017;77:787–793.
14. Mendes Pereira L, Wech T, Weng AM, et al. UTE-SENCEFUL: first results for 3D high-resolution lung ventilation imaging. *Magn Reson Med*. 2019;81:2464–2473.
15. Tibiletti M, Paul J, Bianchi A, et al. Multistage three-dimensional UTE lung imaging by image-based self-gating. *Magn Reson Med*. 2016;75:1324–1332.
16. Josan S, Yen YF, Hurd R, Pfefferbaum A, Spielman D, Mayer D. Application of double spin echo spiral chemical shift imaging to rapid metabolic mapping of hyperpolarized [1-¹³C]-pyruvate. *J Magn Reson*. 2011;209:332–336.
17. Bonanno G, Puy G, Wiaux Y, Van Heeswijk RB, Piccini D, Stuber M. Self-navigation with compressed sensing for 2D translational motion correction in free-breathing coronary MRI: a feasibility study. *PLoS ONE*. 2014;9:e105523.
18. Pallack M, Hricak H, Higgins C, McNamara M, Ehman R. Magnetic resonance imaging with respiratory gating: techniques and advantages. *Am J Roentgenol*. 1984;143:1175–1182.
19. Cheng JY, Zhang T, Ruangwattanapaisarn N, et al. Free-breathing pediatric MRI with nonrigid motion correction and acceleration. *J Magn Reson Imaging*. 2015;42:407–420.
20. Zhang T, Yousaf U, Hsiao A, et al. Clinical performance of a free-breathing spatiotemporally accelerated 3-D time-resolved contrast-enhanced pediatric abdominal MR angiography. *Pediatr Radiol*. 2015;45:1635–1643.
21. Feng L, Axel L, Chandarana H, Block KT, Sodickson DK, Otazo R. XD-GRASP: golden-angle radial MRI with reconstruction of extra motion-state dimensions using compressed sensing. *Magn Reson Med*. 2016;75:775–788.
22. Feng LI, Delacoste J, Smith D, et al. Simultaneous evaluation of lung anatomy and ventilation using 4D respiratory-motion-resolved ultrashort echo time sparse MRI. *J Magn Reson Imaging*. 2019;49:411–422.
23. Jung H, Sung K, Nayak KS, Kim EY, Ye JC. K-t FOCUSS: a general compressed sensing framework for high resolution dynamic MRI. *Magn Reson Med*. 2009;61:103–116.
24. Pang J, Bhat H, Sharif B, et al. Whole-heart coronary MRA with 100 % respiratory gating efficiency: self-navigated three-dimensional retrospective image-based motion correction (TRIM). *Magn Reson Med*. 2014;74:67–74.
25. Rank CM, Heußer T, Wetscherek A, Kachelrieß M. Respiratory motion compensation for simultaneous PET/MR based on strongly undersampled radial MR data. *EJNMMI Phys*. 2015;2(suppl 1):A24.
26. Grimm R, Fürst S, Dregely I, et al. Self-gated radial MRI for respiratory motion compensation on hybrid PET/MR systems. *Med Image Comput Comput Assist Interv*. 2013;16:17–24.
27. Botnar RM, Nekolla SG, Prieto C, Munoz C, Neji R, Kunze KP. Respiratory- and cardiac motion-corrected simultaneous whole-heart PET and dual phase coronary MR angiography. *Magn Reson Med*. 2019;81:1671–1684.
28. Reiner CS, Stolzmann P, Husmann L, et al. Protocol requirements and diagnostic value of PET/MR imaging for liver metastasis detection. *Eur J Nucl Med Mol Imaging*. 2014;41:649–658.
29. Petibon Y, Ouyang J, Zhu X, et al. Cardiac motion compensation and resolution modeling in simultaneous PET-MR: a cardiac lesion detection study. *Phys Med Biol*. 2013;58:2085–2102.
30. Batchelor PG, Atkinson D, Irarrazaval P, Hill D, Hajnal J, Larkman D. Matrix description of general motion correction applied to multishot images. *Magn Reson Med*. 2005;54:1273–1280.
31. Rank CM, Heußer T, Buzan MTA, et al. 4D respiratory motion-compensated image reconstruction of free-breathing radial MR data with very high undersampling. *Magn Reson Med*. 2017;77:1170–1183.
32. Pang J, Chen Y, Fan Z, et al. High efficiency coronary MR angiography with nonrigid cardiac motion correction. *Magn Reson Med*. 2016;76:1345–1353.
33. Prieto C, Doneva M, Usman M, et al. Highly efficient respiratory motion compensated free-breathing coronary MRA using golden-step Cartesian acquisition. *J Magn Reson Imaging*. 2015;41:738–746.
34. Cruz G, Atkinson D, Henningsson M, Botnar RM, Prieto C. Highly efficient nonrigid motion-corrected 3D whole-heart coronary vessel wall imaging. *Magn Reson Med*. 2017;77:1894–1908.
35. Cruz G, Atkinson D, Buerger C, Schaeffter T, Prieto C. Accelerated motion corrected three-dimensional abdominal MRI using total variation regularized SENSE reconstruction. *Magn Reson Med*. 2016;75:1484–1498.
36. Thirion J-P. Image matching as a diffusion process: an analogy with Maxwell's demons. *Med Image Anal*. 2004;2:243–260.
37. Knoll F, Bredies K, Pock T, Stollberger R. Second order total generalized variation (TGV) for MRI. *Magn Reson Med*. 2011;65:480–491.
38. Zhang T, Cheng JY, Chen Y, Nishimura DG, Pauly JM, Vasanaawala SS. Robust self-navigated body MRI using dense coil arrays. *Magn Reson Med*. 2016;76:197–205.
39. Chambolle A, Pock T. A first-order primal-dual algorithm for convex problems with applications to imaging. *J Math Imaging Vis*. 2011;40:120–145.

40. Winkler SA, Corea J, Lechêne B, et al. Evaluation of a flexible 12-channel screen-printed pediatric MRI coil. *Radiology*. 2019;291:180–185.
41. Uecker M, Tamir JJ, Ong F, Lustig M. The BART Toolbox for Computational Magnetic Resonance Imaging. *mricon/bart*: Version 0.5.00. 2019. <https://doi.org/10.5281/zenodo.592960>.
42. Hahn AD, Higano NS, Walkup LL, et al. Pulmonary MRI of neonates in the intensive care unit using 3D ultrashort echo time and a small footprint MRI system. *J Magn Reson Imaging*. 2016;45:463–471.
43. Higano NS, Spielberg DR, Fleck RJ, et al. Neonatal pulmonary magnetic resonance imaging of bronchopulmonary dysplasia predicts short-term clinical outcomes. *Am J Respir Crit Care Med*. 2018;198:1302–1311.
44. Zhang T, Pauly JM, Levesque IR. Accelerating parameter mapping with a locally low rank constraint. *Magn Reson Med*. 2015;66:655–661.
45. Metz CT, Klein S, Schaap M, Van Walsum T, Niessen WJ. Nonrigid registration of dynamic medical imaging data using nD + t B-splines and a groupwise optimization approach. *Med Image Anal*. 2011;15:238–249.
46. Small JH, Flower C, Traill ZC, Gleeson FV. Air-trapping in extrinsic allergic alveolitis on computed tomography. *Clin Radiol*. 1996;51:684–688.

SUPPORTING INFORMATION

Additional supporting information may be found online in the Supporting Information section at the end of the article.

FIGURE S1 Example of motion resolved reconstructions. In the first row are one end expiratory state image from the motion resolved reconstructions. In the second row are the estimated motion field in the S/I direction between the expiratory to inspiratory state

FIGURE S2 Performance comparison among different registration methods. Three different registration methods, Demons, SyN with MSE similarity, and bspline, results are plotted in first row, (A). Difference between aligned image and reference image are plotted in second row, (A). Maximum Intensity Projection of the difference map between aligned image and reference image are shown in (B)

FIGURE S3 aSNRs in three different areas (lung parenchyma, aortic arch, and main airway) with different TGV regularization λ_s levels from one of the cases shown in the Main Text, Figure 6

TABLE S1 Comparison of registration RMSE with different motion resolved reconstruction regularization. As the registration RMSE depends on individual subject scan parameters, motion, etc., measurement of each subject is separately listed. RMSE between two states images before registration is calculated for reference

TABLE S2 Summary of correlation coefficient and mean Euclidean distance of motion fields with different regularizations. As there is no ground truth for motion estimation, we chose the group with only temporal TV regularization as reference for correlation coefficient and mean Euclidean distance calculation. The two metrics are measured in all ($N = 11$) subjects, and the mean and standard deviation are listed

How to cite this article: Zhu X, Chan M, Lustig M, Johnson KM, Larson PEZ. Iterative motion-compensation reconstruction ultra-short TE (iMoCo UTE) for high-resolution free-breathing pulmonary MRI. *Magn Reson Med*. 2020;83:1208–1221. <https://doi.org/10.1002/mrm.27998>